Cell Reports
Physical Science

CellPress
OPEN ACCESS

Article

Bioinspired and biomimetic cancer-cell-derived membrane nanovesicles for preclinical tumor-targeted nanotheranostics

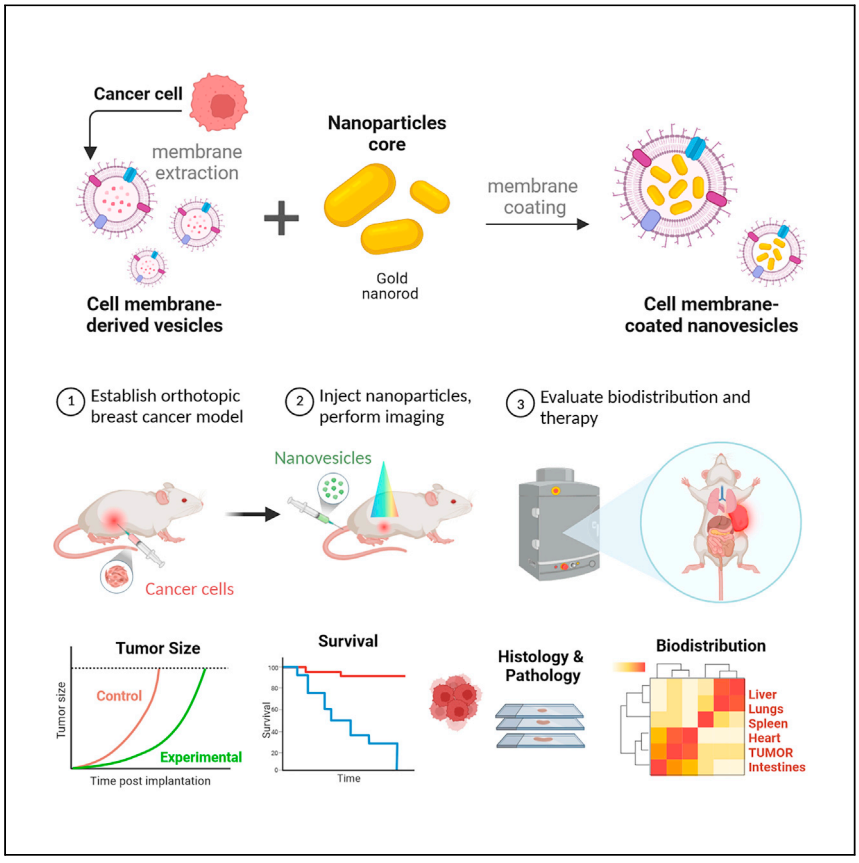

Integrated biomimetic cancer-cell-derived membrane nanovesicles demonstrate localized imaging and synergistic chemo-phototherapeutics for solid tumors. The engineered hybrid system, reported by Prasad et al., demonstrates biocompatibility and safety in pre-clinical breast tumor models without affecting healthy tissues. Better diagnostics and therapeutic response at the minimum dose are key important features of the engineered biomimetic nanovesicles.

Rajendra Prasad, Bárbara B. Mendes, Mahadeo Gorain, ..., Eaint Honey Aung Win, He Qing, João Conde

rajendra.bce@iitbhu.ac.in (R.P.)
joao.conde@nms.unl.pt (J.C.)

Highlights

Effective encapsulation of gold nanorods with cancer-cell-derived membrane vesicles

Bioinspired nanovesicles exhibit better biocompatibility and theranostics response

Integrated biomimetic nanovesicles exhibit localized biodistribution and tumor imaging

Biomimetic nanovesicles demonstrate targeted synergistic therapeutics of solid tumors

Prasad et al., Cell Reports Physical Science 4, 101648
November 15, 2023
https://doi.org/10.1016/j.xcrp.2023.101648

Cell Reports
Physical Science

CellPress
OPEN ACCESS

Article

Bioinspired and biomimetic cancer-cell-derived membrane nanovesicles for preclinical tumor-targeted nanotheranostics

Rajendra Prasad,[1,2,*] Bárbara B. Mendes,[3] Mahadeo Gorain,[4] Gopal Chandra Kundu,[4,5] Narendra Gupta,[6] Berney Peng,[7] Eaint Honey Aung Win,[7] He Qing,[1] and João Conde[3,8,*]

SUMMARY

Bioinspired cell-membrane-camouflaged nanohybrids have been proposed to enhance tumor targeting by harnessing their immune escape and self-recognition abilities. In this study, we introduce cancer-cell-derived membrane nanovesicles (CCMVs) integrated with gold nanorods (AuVNRs) in addition to therapeutic and imaging cargos such as doxorubicin and indocyanine green. This approach enhances targeted tumor imaging and enables synergistic chemo-phototherapeutics for solid tumors. CCMVs demonstrate significant tumor penetration and retention, serving as nanotheranostics with accessible surface biomarkers, biomimicking properties, and homologous targeting abilities. By evading uptake by the mononuclear phagocytic system, CCMVs can diffuse into the deep tumor core, leading to precise tumor reduction while preserving the surrounding healthy tissues. Notably, intravenous administration of these theranostic agents ensures biocompatibility, as evidenced by a survival period of approximately two months (up to 63 days) without any observed side effects. Our findings underscore the diagnostic and therapeutic potential of this biomimetic nanotheranostics platform.

INTRODUCTION

Nanotheranostics, an emerging field of research, focuses on targeted diagnosis and therapeutics in the early stages of cancer.[1–3] It involves integrating diagnostics, therapeutic probes, and targeting ligands at the nanoscale to achieve cellular and tumor selectivity.[4–6] Hybrid theranostics agents, such as liposomes-dye, lipid-gold, polymer-metallic hybrids, silica-gold, gold nanoparticles, and upconversion hybrids, have been extensively investigated for targeted tumor imaging and therapeutics in mouse models.[7–9] However, challenges such as nonspecific biodistribution, lack of site-selective tumor targeting, low tumor accumulation, and suboptimal therapeutic performance still need to be addressed.[5,10,11]

Unsurprisingly, cell membrane-covered nanohybrids and their interventions have garnered significant attention in cancer theranostics research worldwide.[12–14] These hybrid systems, coated with cell membranes, have quickly become standard biomimetics because of their naturally available surface biomarkers, excellent biocompatibility, and improved blood circulation. Among them, nanoparticles coated with red blood cell (RBC)-derived membrane vesicles have gained popularity and have been extensively studied for bioimaging, drug delivery, and cancer therapeutics.[15–17] This popularity stems from their favorable biocompatibility and ease of preparation.

[1]Department of Mechanical Engineering, Tufts University, Medford, MA, USA

[2]School of Biochemical Engineering, Indian Institute of Technology (BHU), Varanasi, Uttar Pradesh 221005, India

[3]ToxOmics, NOVA Medical School|Faculdade de Ciências Médicas, NMS|FCM, Universidade Nova de Lisboa, Lisboa, Portugal

[4]National Centre for Cell Science, Pune 411007, India

[5]School of Biotechnology and Kalinga Institute of Medical Sciences (KIMS), KIIT, Institute of Eminence, Bhubaneswar 751024, India

[6]Trident Diagnostics Center, Trivenee 302015, India

[7]Department of Pathology and Laboratory Medicine, University of California, Los Angeles, Los Angeles, CA 90095, USA

[8]Lead contact

*Correspondence: rajendra.bce@iitbhu.ac.in (R.P.), joao.conde@nms.unl.pt (J.C.)

https://doi.org/10.1016/j.xcrp.2023.101648

However, cell membrane-coated biomimetic nanohybrids or nanotheranostics face significant challenges. These challenges include achieving site-selective tumor targeting with enhanced accumulation, demonstrating effective tumor reduction at low doses (a few tens of milligrams), ensuring reproducibility, and scalability.[18,19] While several convincing approaches have been discussed in the literature, there is still limited understanding of tumor accumulation and cell entry mechanisms.[20–23] Moreover, only a few research groups, including our own, are dedicated to developing clinically relevant nanotheranostics with improved targeting and therapeutics for solid tumors.[24–26] To achieve site-specific targeting of cancer cells within solid tumors, several key considerations must be addressed. First, the injected nanohybrids must evade the formation of a protein corona during blood circulation and prevent prolonged liver retention by bypassing macrophage uptake.[21,22] Second, these nanohybrids need to penetrate the tumor periphery by exploiting leaky blood vessels.[20] Third, they should be capable of navigating the dense and complex extracellular matrix to reach specific cancer cells.[3,27] Last, nanohybrids must overcome the interstitial fluid pressure in the solid tumor environment.[21] Creating nanohybrids to target cells in the heterogeneous tumor microenvironment is an ongoing challenge.[20–22] While diffusion has been widely accepted as a distribution method for nanohybrids within the tumor environment, the dense extracellular matrix hampers diffusion following intravenous and intratumoral administration.[20–23]

Photothermal active nanotheranostics have demonstrated a remarkable ability to enter and penetrate solid tumors with ease when exposed to near-infrared (NIR) light. This effect is primarily attributed to the photothermal expansion and disruption of endothelial cell gaps in leaky blood vessels.[28,29] Based on this understanding, we hypothesized that combining photothermally active therapeutic probes with the inherent soft nature of cancer-cell-derived nanovesicles, which naturally possess surface biomarkers, would facilitate deep tumor penetration and binding to cancer cells.[30] Additionally, the utilization of small photothermally active gold nanorods is expected to significantly enhance the nanotheranostic system because previous studies have reported improved uptake by cells and tumors.[31–33]

In this study, we present a bioinspired targeted theranostic agent designed specifically for solid tumor imaging and therapy (Scheme 1). Our approach involves the utilization of biomimetic nanovesicles derived from cancer cells, known as cancer-cell-derived membrane nanovesicles (CCMVs), which are carefully adorned with gold nanorods (AuNRs). The resulting hybrid entities, termed AuVNRs, exhibit excellent capabilities because they not only serve as carriers for fluorescent imaging probes like indocyanine green (ICG) dye but also have the ability to encapsulate potent chemotherapeutic drugs such as doxorubicin (DOX). This engineered system enables noninvasive imaging of solid tumors and exerts synergistic therapeutic effects upon exposure to NIR light. Through the strategic integration of photothermally active components, we observed a significant reduction in solid tumors when subjected to NIR light illumination. This outcome can be attributed to the dual mechanisms at play. First, the AuVNRs generate photothermal heat, which exerts a localized hyperthermic effect within the tumor microenvironment. Second, the NIR light triggers the controlled release of the loaded anticancer drug DOX, specifically targeting cancer cells within the heterogeneous breast tumor environment. One of the key advantages of this innovative approach is the selective nature of tumor reduction with minimal impact on the surrounding healthy tissues. This observation underscores the therapeutic potential and localized effectiveness of our engineered biomimetic hybrid system. By harnessing the inherent properties of cancer-cell-derived nanovesicles, along with the unique capabilities of AuNRs, we successfully

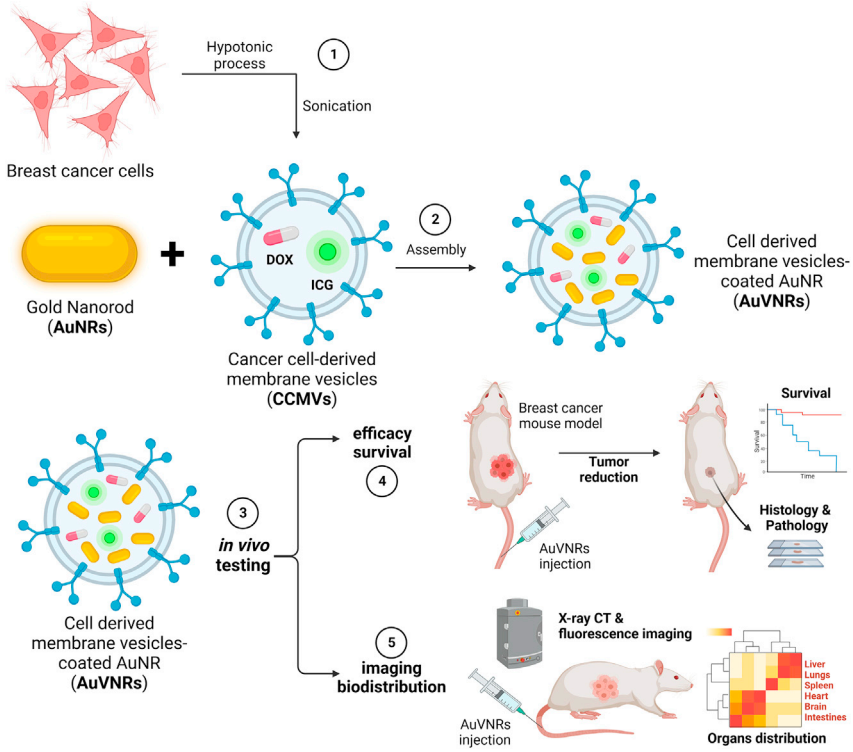

Scheme 1. Methodological strategy for the development of CCMVs for preclinical tumor-targeted nanotheranostics in breast cancer

(1) To obtain nanosized cell-derived vesicles, 4T1 breast cancer cells were treated with a hypotonic suspension and then sonicated. (2) These CCMVs, loaded with the drug (DOX [doxorubicin]) or the fluorescent dye (ICG [indocyanine green]), enable the decoration of surface-modified AuNRs, facilitating their targeted delivery to cancer cells. (3) The functionality of AuNR-encapsulated vesicles (AuVNRs) was evaluated *in vivo* using breast cancer mouse models. The assessment included (4) analyzing animal efficacy survival to determine the therapeutic effectiveness and (5) examining imaging biodistribution to understand the localization of the fluorescent imaging agent. This approach aims to enhance the precision and effectiveness of drug delivery to breast cancer cells, allowing a comprehensive evaluation of AuVNRs' therapeutic potential and imaging capabilities for translational applications in breast cancer nanomedicine.

created a multifunctional platform that holds promise for targeted theranostics in solid tumor management.

RESULTS

CCMVs efficiently coat the AuNR surface

To achieve uniform plasmonic AuNRs, controlled addition of hydroquinone was carried out in the presence of N-cetyltrimethylammonium bromide (CTAB) surfactant, silver nitrate-mediated growth solution, hydrochloric acid, and ascorbic acid. This process yielded AuNRs with a monodispersed size distribution of 34 $\pm$ 2 nm in length and 11 $\pm$ 1 nm in width, as confirmed by transmission electron microscopy (TEM) analysis (Figure 1A). The size distribution was further validated by the presence of narrow peaks in the absorption spectra at 519 nm (transverse peak) and 800 nm (longitudinal peak) (Figure 1D). Additionally, the aqueous dispersion of AuNRs exhibited a visible homogeneity, as observed in the TEM image (Figures 1A, inset; S1A; and S1B).

Biomimetic CCMVs were derived from mouse breast cancer cells (4T1 cell line) via hypotonic cell lysis and self-assembly, followed by mild sonication. The resulting

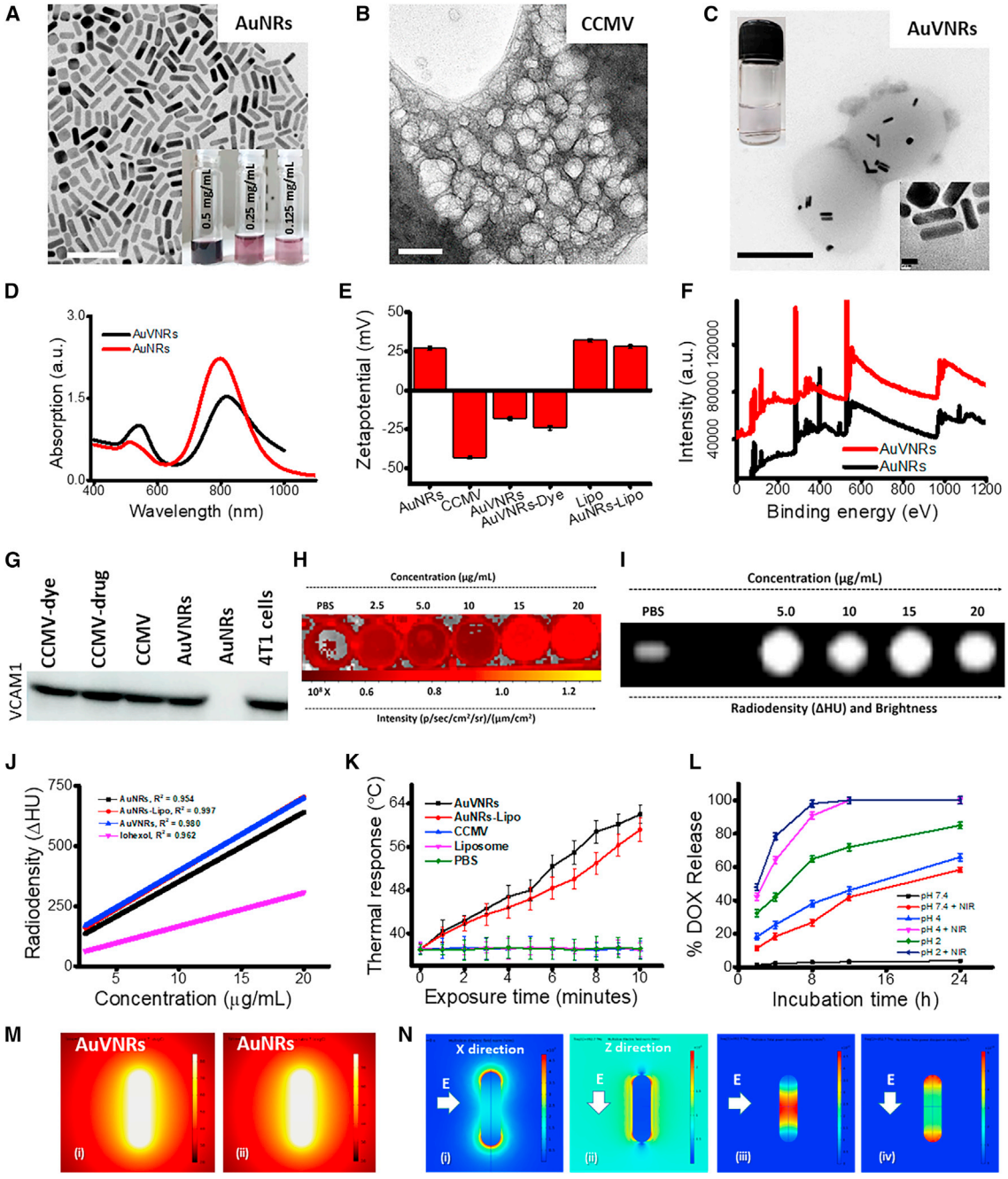

Figure 1. Physico-chemical properties of AuVNRs and related nanoparticles

(A–C) TEM images of (A) CTAB-stabilized gold nanorods (AuNRs), (B) cancer-cell-derived membrane nanovesicles (CCMVs), and (C) AuNR-encapsulated CCMVs (AuVNRs) containing dispersion solution at 0.125 mg/mL (inset, digital image).

(D) Absorption spectra of AuNRs and AuVNRs.

(E) Surface charge measurement of AuNRs, AuVNRs, liposomes (Lipos), and related formulations.

(F) XPS spectra showing atomic Au peaks at 82.2 eV for Au $4f_{7/2}$ and 86 eV for Au $4f_{5/2}$ of Au^0 of AuNRs and AuVNRs.

(G) Western blot analysis to further demonstrate the successful decoration of AuNRs with cell membranes from 4T1 cells using VCAM1 (vascular cell adhesion molecule 1) as a specific cell membrane marker present on the surface of these breast cancer cells.

(H and I) *In vitro* NIRF (H) and radio density (I) through X-ray CT of PBS and AuVNRs at different concentrations.

(J) Radiodensity measurements (namely, R^2 values) were 0.962 (iohexol), 0.954 (AuNRs), 0.997 (AuNRs-Lipo), and 0.980 (AuVNRs).

(K) Time-dependent photothermal transduction of AuVNRs and AuNRs-Lipo using an 800-nm NIR laser source (1 W power).

Figure 1. *Continued*
(L) Time-dependent drug DOX release kinetics with and without NIR light (800 nm, 1 W) exposure.
(M) COMSOL-simulated 3D model of AuNRs and AuVNRs.
(N) Photothermal response of AuVNRs with the finite element method (FEM).
Scale bars: 50 nm (B), 200 nm (C and D), and 5 nm (D, inset). All error bars are reported as standard deviation (SD).

CCMVs, at 800 mg/batch (4.9×10^{13} nanovesicles/mL), showed a spherical morphology and a uniform size of 95 ± 5 nm as evaluated by low-cryo-mode TEM (Figure 1B). The CTAB surfactant from AuNRs was replaced by CCMV layers, and then these surface-modified nanorods were encapsulated in CCMV spherical nanoparticles named AuVNRs (Figures 1B and 1C). CCMV-coated AuNRs had a greater width of 0.5 ± 0.1 nm compared with the original width (Figure 1C, inset). The first step of our study involved surface modification of AuNRs using vesicle membranes. This modification resulted in an increase in the width, as shown in Figures 1A and S1D, where the modified nanorods exhibited a width of 11.5 nm compared with the original width of 11 nm. This increase in width was expected, considering the additional thickness contributed by the vesicle membranes. Subsequently, the surface-modified nanorods were encapsulated within nanovesicles derived from cancer cells. This encapsulation process is evident in the TEM images, which show the presence of modified nanorods within the cancer-cell-derived nanovesicles. By incorporating vesicle membranes and encapsulating the modified nanorods within cancer-cell-derived nanovesicles, our study aimed to harness the unique properties and capabilities of these composite structures for further investigation and potential applications. These findings highlight the successful surface modification of AuNRs and their subsequent encapsulation within cancer-cell-derived nanovesicles, as visualized by TEM imaging. These morphological differences were corroborated by absorption spectroscopic measurements, where peak broadening and a redshift (from 800 to 818 nm) in the longitudinal and transverse peaks were observed (Figure 1D). Moreover, the surface engineering of the AuNRs was confirmed by surface charge measurements (Figure 1E). AuVNRs exhibited a negative surface charge (-18 ± 3 mV), which indicates that the CCMV-supported AuNRs were efficiently encapsulated in the nanovesicles. In contrast, AuNRs possessed a positive surface charge of $+27 \pm 2$ mV, primarily because of the presence of the cationic CTAB surfactant, while CCMVs exhibited an anionic (-43 ± 5 mV) surface charge. AuVNRs demonstrated better aqueous dispersion than particles based solely on AuNRs because of their negative surface charge, which indicates better colloidal stability of the engineered AuVNRs (Figure 1C, inset). Moreover, the aqueous dispersion of AuVNRs remained stable even after 30 days of storage (Figures S1A and S1B). The hydrodynamic diameters of the AuVNRs in aqueous solution were in the range of 100–140 nm at different time points (days 1, 7, 14, and 30) (Figure S1C). Free nanorods that were not taken up by the vesicles were removed by centrifugation (10,000 rpm for 20 min at 20°C). During centrifugation, the supernatant (with free nanorods) was discarded, and CCMVs (with nanorod-encapsulated CCMVs) settled down in the form of pellets because of their high density compared with free nanorods and CCMVs (Figures S1D–S1F). The obtained pellet of nanorod-encapsulated CCMVs was washed thoroughly with Milli-Q water and PBS (pH 7.4) and dialyzed. The characteristics of atomic Au peaks were confirmed by X-ray photoelectron spectroscopy (XPS) attributed to 82.2 eV for Au $4f_{7/2}$ and 86 eV for Au $4f_{5/2}$ of Au^0 (Figures 1F and S2A). The presence of a characteristic N 1s peak at 400 eV in AuNRs and AuVNRs was clearly seen in the XPS spectra, where the N 1s peak at 400 eV in AuNRs was very much dominant compared with AuVNRs because of the abundant CTAB present in AuNRs. However, the presence of the N 1s peak at 400 eV in the AuVNRs with a red shift indicates the surface modification of the AuNRs (Figure S2B).

For imaging purposes, an NIR fluorescent (NIRF) imaging dye (ICG[34]) was loaded onto the CCMVs and liposomal formulations. These formulations were further assembled with AuNRs to create ICG dye-loaded AuVNRs (AuVNRs-Dye) and ICG dye-loaded AuNRs-liposomes (AuNRs-liposome [Lipo]-Dye). The characterization of these formulations was performed using TEM, UV-visible (UV-vis)-NIR absorption spectroscopy, and surface charge zeta potential techniques (Figures 1 and S3). Free ICG dye in water suspension showed an absorption of approximately 780 nm, whereas Lipo-Dye and CCMVs-Dye showed absorption of 785–788 nm (Figure S3). In UV-vis-NIR absorption spectroscopic measurements, ICG dye-loaded nanoparticle formulations were characterized by a broad scattering between 200 and 400 nm compared with the free ICG dye. Interestingly, upon ICG dye incorporation, AuVNRs showed NIRF because of ICG fluorescence (Figure 1H) as well as radiocontrast performance because of the high atomic number and X-ray attenuation of gold (Figure 1I). Augmented fluorescence intensity (under 750-nm excitation) and radiocontrast (100 kVp [x-ray tube voltage]) with better brightness were observed with respect to the concentrations (2.5–20 $\mu g\ mL^{-1}$) of the designed AuVNRs (Figures 1J and S3). A significant difference in the fluorescence characteristics was observed between free ICG dye and ICG dye encapsulated within AuVNRs. The free ICG dye exhibited lower emission and brightness as the concentration or number of molecules increased (Figure S4). This decrease in fluorescence intensity can be attributed to self-quenching, which compromises the photostability of the dye. Conversely, when ICG dye was encapsulated within the AuVNRs, significantly improved red fluorescence was observed. This enhancement in fluorescence can be attributed to the aggregation of ICG molecules within the AuVNR cavity. This aggregation not only prevents self-quenching, but also facilitates the efficient emission of red fluorescence. The differential fluorescence responses between free ICG dye and ICG dye encapsulated within AuVNRs emphasize the advantages of the encapsulation approach. By utilizing AuVNRs as a carrier, we can overcome the photostability issues associated with free ICG dye and achieve a more robust and enhanced red fluorescence response. Furthermore, the homogeneous signal intensity with linear correlation from AuVNRs at different concentrations indicated a quenching-free environment and uniform distribution of ICG during AuVNR assembly (Figure 1J), which led to the use of AuVNRs as a unique contrast agent for nanoparticle tracking and deep-core imaging of solid tumors. On the other hand, to demonstrate nanovesicle formation around AuNRs, a western blot analysis was carried out to demonstrate the successful decoration of AuNRs with cell membrane from 4T1 cells using VCAM1 (vascular cell adhesion molecule 1) as a specific cell membrane marker present on the surface of these breast cancer cells (Figure 1G). By incorporating VCAM1 into the engineered nanotheranostics, these particles gain the ability to specifically recognize and bind to cancer cells that express VCAM1, leading to enhanced tumor targeting and selective delivery of therapeutic agents or imaging probes to tumor tissues. The results of the western blot revealed a distinct and prominent band corresponding to VCAM1 in the lanes representing the AuNRs coated with the 4T1 cell membrane (AuVNRs), similar to patterns for 4T1 cells only and CCMVs alone. In contrast, the control lanes containing uncoated AuNRs exhibited no significant band for VCAM1. This difference in band intensity clearly confirmed the successful decoration of AuNRs with the 4T1 cell membrane, specifically targeting VCAM1.

The prepared nanorods (AuVNRs and AuNRs-Lipo) were tested under NIR light exposure (800 nm, 1 W, 10 min) to evaluate their photothermal response resulting from localized surface plasmon resonance (Figures 1K and S5). Within 6 min of NIR light exposure, the AuVNRs and AuNRs-Lipo demonstrated significant

photothermal responses, with recorded hyperthermia (43°C) and ablation temperatures exceeding 45°C (Figures 1K, S5A, and S5B). This thermal performance was further supported by simulation studies (Figures 1M, 1N, S5C, and S5D), where 3D models of AuNRs (8.8 × 32.8 nm dimension) were modeled. Following the demonstration of photothermal response, the release kinetics of DOX were investigated under various conditions in the absence or presence of NIR light (Figure 1L). Interestingly, a burst release of DOX from AuVNRs-DOX was observed under low pH conditions and NIR light irradiation (800 nm, 1 W, 10 min), with maximum release (more than 85% ± 5%) occurring within 4 h. In contrast, at neutral pH, a low amount of DOX was released from AuVNRs-DOX after 12 h. The significant drug release observed after NIR light exposure can be attributed to a photothermally triggered effect that ruptures the soft drug carriers (i.e., CCMVs). The soft nature of the CCMVs, attributed to the presence of lipid bilayers and flexible membrane components, renders them susceptible to thermally induced changes. The elevated temperature resulting from the photothermal effect disrupts the structural integrity of the CCMVs, leading to the rupture of the lipid bilayers and the subsequent release of the encapsulated DOX. This photothermally triggered effect provides a precise and controlled means of drug release because it can be selectively activated by NIR light at the tumor site, minimizing off-target effects and maximizing therapeutic efficacy.

AuVNRs demonstrated high biocompatibility and *in vitro* targeted theranostic performance

To comprehensively assess the efficacy of the designed nanotheranostics for cancer therapeutics, a two-pronged approach was adopted, considering normal and cancer cell models. Initially, NIH3T3 normal fibroblast cells were specifically selected to evaluate the cytotoxicity of the engineered nanotheranostics. This choice is crucial because it allows us to assess the potential toxic effects of nanotheranostics on non-cancerous, healthy cells, providing important insights into their safety profiles. For the assessment of targeted cancer cell imaging and therapeutic response, a breast cancer cell line, 4T1 cells, was strategically chosen. This cell line was specifically employed to examine the cellular uptake and cytotoxicity of the engineered AuVNRs-Dye in cancer cells. The selection of breast cancer cell lines is particularly relevant because they represent a commonly studied model for breast cancer research and offer insights into the behavior and response of nanotheranostics in a disease-specific context. By incorporating normal and cancer cell models into our evaluation, we can gain a comprehensive understanding of the cytotoxicity, targeted imaging capability, and therapeutic response of engineered nanotheranostics. To assess the viability of healthy NIH3T3 cells (a murine fibroblast cell line) in the presence of increasing concentrations of nanoparticles (up to 500 μg mL^{-1}), a 3-(4,5-dimethylthiazol-2-yl)-2,5-diphenyl-tetrazolium bromide (MTT) assay was performed after 24 h (Figure 2A). The CCMV and Lipo-based formulations exhibited more than 80% ± 5% cell viability, while the AuNRs demonstrated less than 50% ± 5% cell viability because of the toxic nature of the CTAB surfactant. Different nanostructures were loaded with the anticancer drug DOX, and AuNRs were assembled within these nanostructures. Additionally, western blot analysis was carried out for CCMVs, AuVNRs, AuNRs and DOX tagged ICG dye encapsulated AuVNRs nanoparticles treated 4T1 cells (Figure 2B). The engineered nanoparticles induced apoptosis, as validated through western blot analysis using specific antibodies against well-known markers, PARP1 (poly-ADP ribose polymerase 1) and Cyclin D1. The expression of the cell proliferative marker Cyclin D1 was reduced in cells treated with CTAB-attached AuNRs and DOX-loaded AuVNRs because of the toxic effects of DOX and CTAB surfactant. In contrast, cancer cells treated with CCMVs

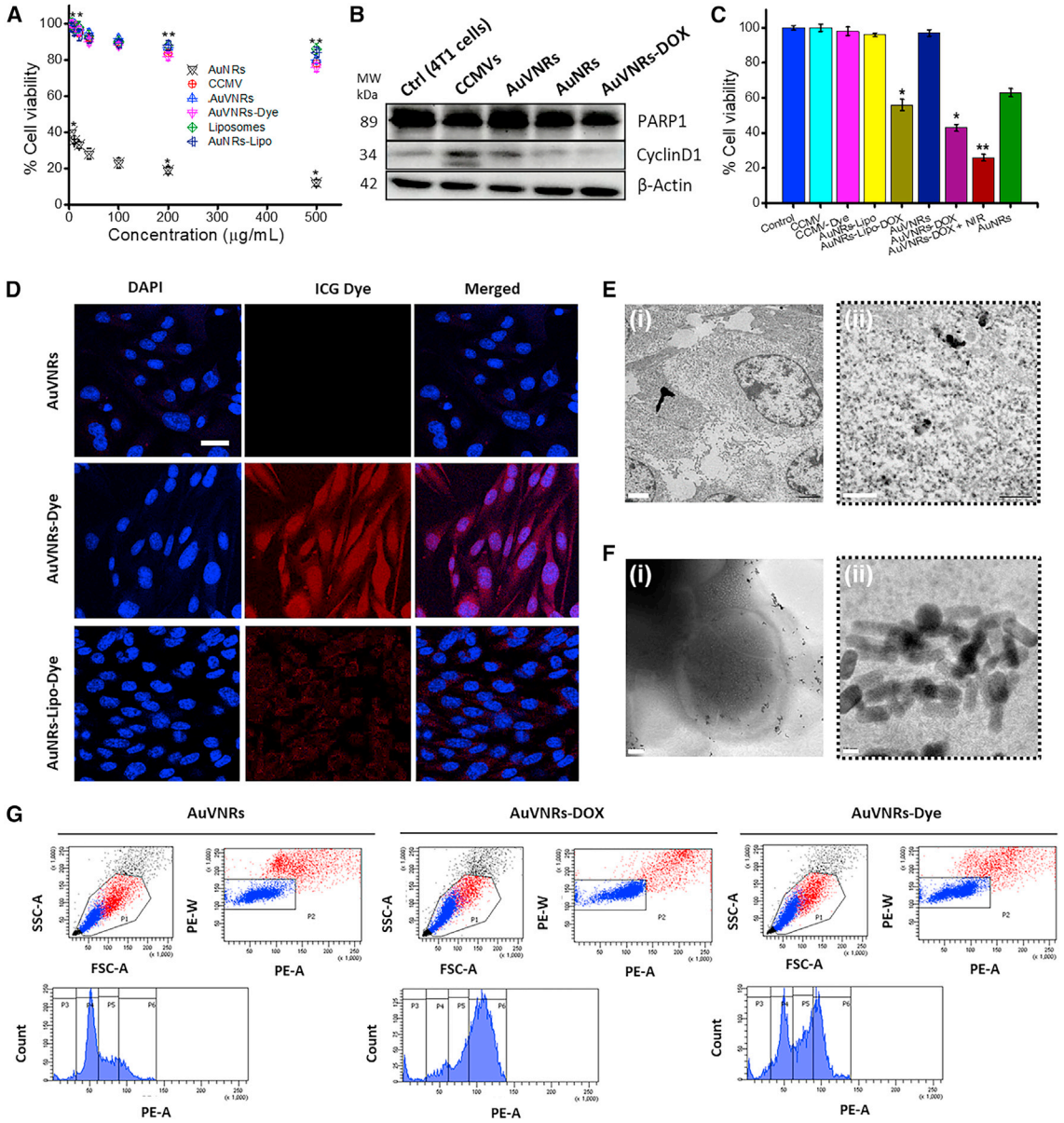

Figure 2. ***In vitro*** **viability and theragnostic performance of the AuVNRs and related nanoparticles**

(A) Cell viability of NIH3T3 cells to increasing concentrations (50–500 μg mL^{-1}) of AuNRs, AuVNRs, CCMVs, Lipos, gold nanorods supported Lipos (AuNRs-Lipo), and dye-loaded AuVNR nanoparticles.

(B) Western blot validation using 4T1 breast cancer cells treated with free CCMVs, AuVNRs, AuNRs, and ICG-AuVNRs-DOX (150 μM) for 24 h and expression of the apoptotic markers PARP1 and CyclinD1 using their specific antibodies. 4T1 cells without any treatment were used as a control. β-Actin was used as a loading control because is expressed within all eukaryotic cell types and is not affected by cellular treatments.

(C) *In vitro* therapeutic assessment of engineered nanotheranostics such as AuNRs, CCMVs, ICG dye-loaded CCMVs (CCMVs-Dye), AuNRs-Lipo and AuNRs-Lipo-DOX, AuVNRs and AuVNRs-DOX, and NIR-exposed AuVNRs-DOX on breast cancer cells at 100 μg mL^{-1}. Mean ± SD. Statistical significance: *$p < 0.05$ and **$p < 0.001$.

(D) *In vitro* breast cancer cell targeting and uptake ability of AuVNRs, AuVNRs-Dye, and AuNRs-Lipo-Dye using confocal microscopy analysis.

(E and F) Bio-TEM images of AuVNR-treated cancer cells (E) before and (F) after NIR light treatment (10 min of 800-nm light exposure).

(G) Flow cytometry analysis (side scattering [SSC-A] versus forward scattering [FSC-A]) of AuVNR-, AuVNRs-Dye-, and AuNRs-Lipo-Dye-treated cancer cells.

Scale bars: 50 μm (D), 2 μm (E-i), 500 nm (E-ii), 0.2 μm (F-i), and 10 nm (F-ii). Staining: DAPI (blue) and ICG dye (red). All error bars are reported as SD.

and AuVNRs exhibited clear bands of Cyclin D1, which were almost similar to the control group consisting of only 4T1 cells without any treatment. This significant observation indicated a clear difference between AuNRs and AuVNRs. Furthermore, the western blot data demonstrated a downregulation in the level of PARP after treatment with the engineered therapeutic nanoparticles, indicating the cleavage of full-length PARP, a marker of apoptosis.

The cellular uptake of AuVNRs-dye was tested using the 4T1 breast cancer cell line. As shown in Figure 2C, no cell death was observed in the drugless formulations, whereas more than 50% cell death was observed in drug-loaded nanorod-treated cancer cells. After the NIR light-treated therapeutic course, cell death increased by more than 75%, demonstrating the synergistic chemo-phototherapeutic ability of the designed biomimetic theranostics. The biomimetic dye-tagged theranostic system was further examined for targeted cancer cell imaging at different incubation times (3 h, 6 h, and 12 h), with the optimal incubation time for deep cellular internalization determined to be 6 h (Figure S6). Moreover, this formulation exhibited deep cellular internalization within 6 h of treatment, displaying a higher fluorescence signal intensity compared with AuNRs-Lipo-Dye (Figure 2D). Following NIR light irradiation, an enhanced emission response from the interior of the cell indicated the photothermal disruption of the cancer cell membrane and rapid uptake of surface-engineered AuNRs (Figures S7 and S8), which correlated with bio-TEM images showing the presence of AuVNRs within cancer cells (Figures 2E and 2F). The fluorescence and pixel intensities of AuVNRs-Dye- and AuVNRs-DOX-treated 4T1 cells in the red channel are shown in Figure S8. In flow cytometry validation, two modes of scattering, the side-scattering channel (SSC) and the forward-scattering channel (FSC), were utilized to assess the cellular uptake of the nanotheranostics. In the SSC mode, higher signal intensities were observed in the AuVNRs-Dye-treated cancer cells compared with the AuNRs-Lipo-Dye-treated cancer cells, indicating superior uptake of AuVNRs in breast cancer cells (Figure 2G). The scattered light collected in the SSC mode provides insights into the cell's internal complexity. When AuVNRs nanoparticles are internalized into the cells, the internal complexity of the cells increases, resulting in a noticeable intensity in the SSC mode. This suggests that the AuVNRs are effectively taken up by the cancer cells, leading to enhanced scattering signals in the SSC mode. In contrast, the FSC intensities of the nanoparticle-treated cancer cells were comparable with those of the control groups (cells and nanoparticles without dye encapsulation). The FSC mode primarily captures the forward-scattered light, which is influenced by the size and granularity of the cells. The similar FSC intensities between the treated and control groups suggest that the size and granularity of the cells remain largely unchanged upon exposure to the nanotheranostics. These observations highlight the differential scattering patterns in the SSC and FSC modes, reflecting the internal complexity and cell size/granularity, respectively. AuVNRs-Dye demonstrated better cell uptake than AuNRs-Lipo-Dye, mainly because of the presence of surface biomarkers and the inherent targeting ability of CCMVs (Figure 2G). The higher SSC signal intensities in the AuVNRs-Dye-treated cancer cells indicate enhanced uptake and internalization of the AuVNRs, underscoring their potential as effective theranostic agents for breast cancer treatment.

In addition, hemolysis measurements were conducted to ensure the biocompatibility of the different formulations in the absence and presence of DOX at various concentrations (50–500 $\mu g\ mL^{-1}$) (Figure S9). At 12 h, significant hemolysis (95% $\pm$ 10%) was observed in free DOX and AuNR formulations, while minor hemolysis (less than 6%) was observed in the other studied formulations. This significant

difference in hemolysis can be attributed to the toxic nature of the anticancer drugs and CTAB surfactant present in the free DOX and AuNR formulations. The toxic components lead to adverse effects on RBCs and result in a high hemolysis rate. On the other hand, the surface-modified AuNR formulations exhibited improved biocompatibility, as indicated by the negligible hemolysis observed. The minimal interaction between the surface-masked AuNRs and the RBCs contributed to favorable hemocompatibility outcomes. This finding suggests that the surface modifications effectively reduce the toxic effects and interactions between the nanoparticles and the RBCs, enhancing the biocompatibility of the formulations. This enhanced biocompatibility of the surface-modified AuNR formulations paves the way for their potential application in *in vivo* studies. The minimal interaction with normal cells further supports the promising potential of AuVNRs as nanotheranostic agents, offering improved cellular uptake and therapeutic response compared with AuNRs-Lipo formulations.

Gold nanovesicles demonstrated *in vivo* targeted tumor imaging and selective biodistribution

Gold nanovesicles, such as AuVNRs-Dye and AuNRs-Lipo-Dye, were intravenously administered to BALB/c mice bearing solid tumors. The circulation of the injected nanoparticles was examined by collecting blood samples at various time points (1, 2, 4, 6, 8, 10, 12, and 24 h), and the gold content was quantified using inductively coupled plasma-mass spectrometry (Figure S10). The blood circulation half-life ($t_{1/2}$) was calculated to be approximately 5.2 $\pm$ 0.5 h, which is consistent with previously reported systems,[35] further confirming the consistency of the observed circulation kinetics. By understanding the circulation dynamics, we gain insights into the behavior of these gold nanovesicles within the bloodstream, providing essential information for their potential applications in targeted imaging and therapy.

To assess the biodistribution and targeted imaging of solid tumors, mice were scanned using whole-body X-ray computed tomography (CT) (Figure 3A) and NIRF imaging (Figure 3B) 1, 24, and 48 h post injection. The imaging scans clearly visualized the tumors in the post-injection animals, and the contrast was significantly different from the pre-injection animals (Figures 3B and S11). Notably, AuNRs-Lipo-Dye exhibited substantial accumulation in the liver and spleen for up to 48 h, with consistent contrast signals over the duration of the experiment; especially the liver accumulation showed Δ83 Hounsfield units (HU) and 0.78 $\times$ 10^8 p/s/cm^2/sr after 1 h, Δ65 HU and 0.69 $\times$ 10^8 p/s/cm^2/sr after 24 h, and Δ59 HU and 0.61 $\times$ 10^8 p/s/cm^2/sr after 48 h. In contrast, AuVNRs-Dye showed a minimum liver accumulation 1 h post injection (Δ75 HU from X-ray CT and 0.16 $\times$ 10^8 p/s/cm^2/sr from NIRF), which gradually decreased over time; namely, Δ32 HU and 0.10 $\times$ 10^8 p/s/cm^2/sr after 24 h and Δ28 HU and 0.053 $\times$ 10^8 p/s/cm^2/sr after 48 h. Moreover, AuVNRs-Dye exhibited enhanced contrast values from the tumor area as the post-injection time increased. X-ray CT scans of the post-injection animals highlighted that AuVNRs-Dye displayed lower radiodensity in major organs compared with AuNRs-Lipo-Dye, demonstrating the superior targeting ability of AuVNRs.

These imaging results provide strong evidence of the targeted accumulation of AuVNRs-Dye in solid tumors while minimizing their accumulation in the liver. The low radiodensity observed in major organs further supports the enhanced targeting ability of AuVNRs. These findings emphasize the potential of AuVNRs as an effective and precise imaging agent for solid tumor diagnosis, offering improved targeting capabilities compared with AuNRs-Lipo-Dye.

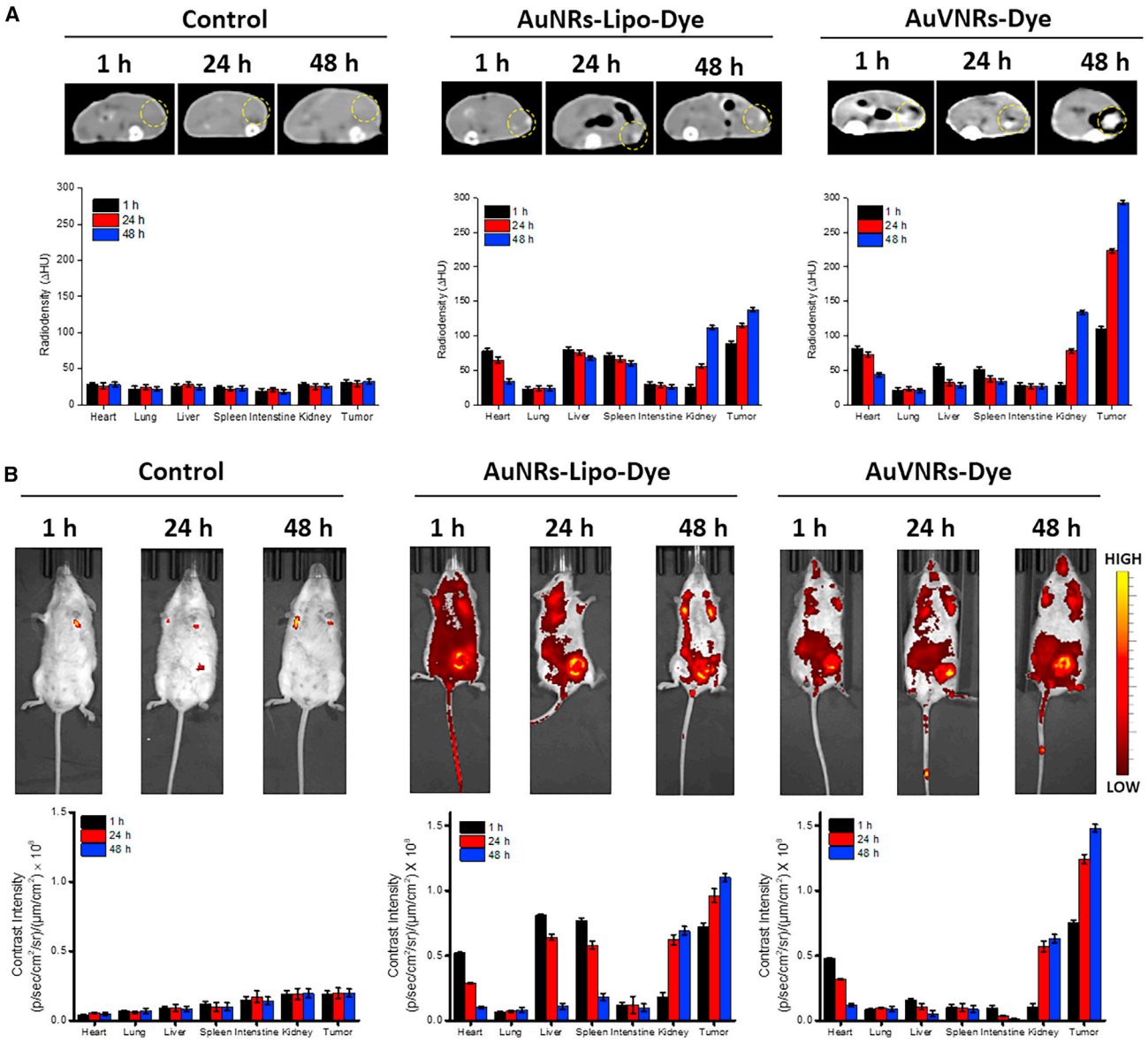

Figure 3. Time-dependent and bio-distribution analyses of pre-injection animals (as a control) and intravenously injected AuVNRs-Dye and AuNRs-Lipo-Dye

(A) An axial view of X-ray CT images of AuVNRs-dye and AuNRs-Lipo-dye compared with pre-injection animals (control).

(B) Whole-body NIRF imaging of targeted solid tumor imaging and biodistribution profile of the injected nanostructures. All error bars are reported as SD.

Following the injection of gold-based nanoparticles, the animals were euthanized after 48 h, and all tissues, including the tumors, were collected for *ex vivo* X-ray CT scans. In the case of animals treated with AuVNRs-Dye, a significant contrast was observed from the tumor region, indicating the targeted accumulation of these nanoparticles within the tumor site. Conversely, AuNRs-Lipo-Dye exhibited maximum contrast signals from the liver and spleen, with negligible signals from the tumor area, highlighting their limited binding ability to tumors (Figures 4A–4C). This difference in contrast values clearly demonstrates the superior tumor binding ability of AuVNRs-Dye, which can be attributed to their naturally available surface biomarkers. These surface biomarkers enable the nanoparticles to avoid

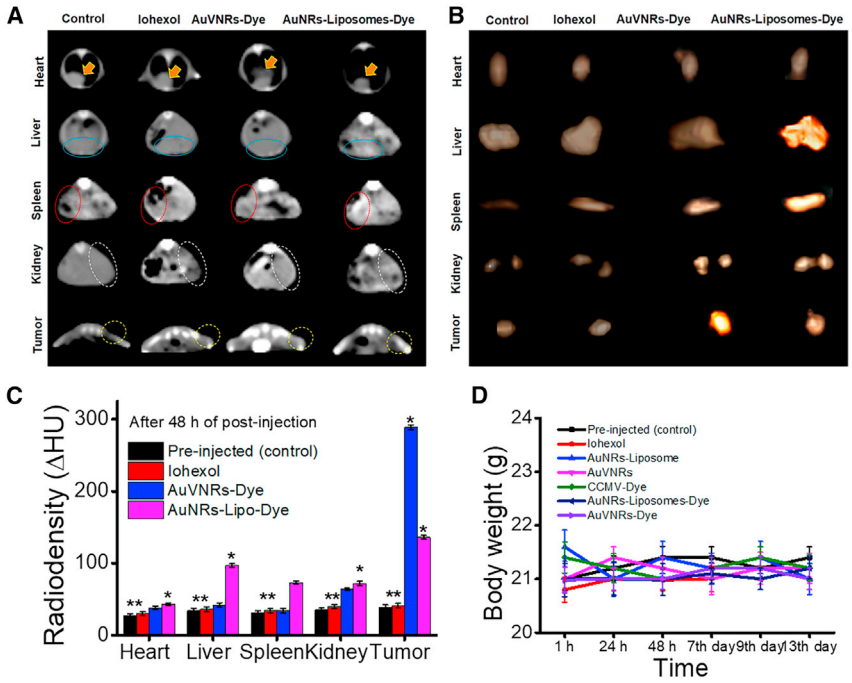

Figure 4. Tumor targeting and radio density measurements

(A) An axial view of X-ray CT images of major organs (heart, liver, spleen, and kidneys) and tumors measured from AuVNRs-dye-, AuNRs-Lipo-dye-, and iohexol-injected animals compared with pre-injection animals (control). Heart location is indicated by solid yellow arrows, solid blue circles represent the liver site, red dotted circles indicate the spleen, white dotted circles indicate the kidney location, and light yellow dotted circles indicate the tumor site.

(B and C) *Ex vivo* X-ray CT scans of collected organs (heart, liver, spleen, and kidneys) and tumors 48 h of post injection of AuVNRs-dye, AuNRs-Lipo-dye, and iohexol and compared with pre-injected animals (control) (B) and their radio density measurements (C).

(D) Time-dependent body weight measurements of AuVNR-, AuVNRs-dye-, AuNRs-Lipo-, AuNRs-Lipo-dye-, CCMV-dye-, and iohexol-injected animals compared with pre-injected animals (control). All error bars are reported as SD.

macrophage uptake and facilitate recognition by cancer cells, enhancing their tumor-specific targeting.

Importantly, the injected nanoparticles did not induce any noticeable changes in the body weight of the animals throughout the 2-week observation period, indicating their excellent biocompatibility and lack of systemic toxicity (Figure 4D). This finding further supports the favorable safety profile of the nanoparticles, making them promising candidates for biomedical applications. The distinct contrast values observed between AuVNRs-Dye and AuNRs-Lipo-Dye highlight the unique characteristics of AuVNRs-Dye, including their surface biomarkers and soft nature. These attributes allow them to easily penetrate the complex environment of solid tumors, facilitating their targeted accumulation and imaging.

AuVNRs showed a targeted synergistic therapeutic for solid tumor reduction

The targeted synergistic therapeutic effect of AuVNRs in reducing solid tumors was evaluated in a study involving four groups of tumor-bearing animals. Female mice with 4T1 tumors were intravenously injected with AuVNRs-DOX and AuNRs-Lipo-DOX (Figure 5A). 1 h post injection, these animals were exposed to NIR light (800 nm for 10 min), which was repeated five times at 3-day intervals. The tumor volume was measured and recorded (Figure 5B). A significant reduction in tumor

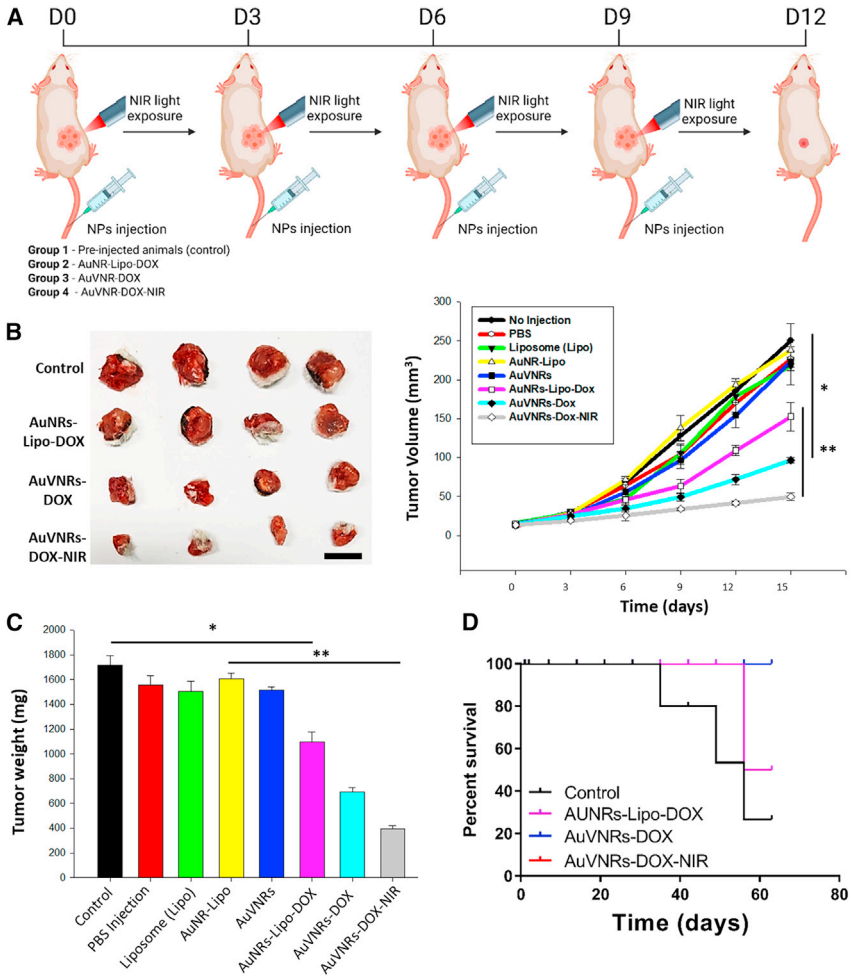

Figure 5. Targeted synergistic therapeutic efficacy of AuVNRs-DOX and AuNRs-Lipo-DOX theranostic nanoparticles for solid tumor reduction

(A) Scheme of the *in vivo* experimental design.

(B) Volume tumor measurements over therapeutic evaluation for control (pre-injection animals), AuNRs-Lipo-DOX, AuVNRs-DOX with and without NIR light treatment. Inset: digital photographs of collected tumors after treatments of Liposomes (Lipo), AuNR-Lipo, AuVNRs, AuNRs-Lipo-DOX, AuVNRs-DOX, and NIR exposed AuVNRs-DOX.

(C) Tumor weight measurements of obtained tumors after different therapeutics courses. Mean ± SD. Statistical significance: **$p < 0.01$, one-way ANOVA with Kruskal-Wallis multiple-comparisons test.

(D) Time-dependent animal survival pattern (checked up to 63 days). Scale bar: 1 mm (B). All error bars are reported as SD.

volume (30.4 and 49 mm^3) and weight (397 and 395 mg) was observed in tumor-bearing mice treated with AuVNRs-DOX followed by NIR light exposure. This decrease can be attributed to the synergistic therapeutic effect of the released DOX and the generated photothermal heat. In stark contrast, pre-injection tumor-bearing animals exhibited significantly larger tumor volumes (168 and 250 mm^3) and weights (862 and 1,718 mg). These findings underscore the effectiveness of engineered nanotheranostics in achieving tumor reduction through the combined action of chemotherapy and photothermal therapy. In terms of tumor weight reduction, AuVNRs-DOX demonstrated better results (36.1% ± 8.3%) compared with AuNRs-Lipo-DOX (24.6% ± 9.2%), highlighting the chemotherapeutic effect of AuVNRs on solid tumors (Figure 5C). Furthermore, when NIR light treatment was

applied, AuVNRs-DOX exhibited a significant tumor reduction (63.8% ± 4.6%) compared with AuNRs-Lipo-DOX and AuVNRs-DOX without NIR light. This can be attributed to the production of photothermal heat and the phototriggered release of DOX in the tumor environment, emphasizing the impact of synergistic therapy provided by a single nanotheranostic system. Notably, tumor volumes exceeding 250 mm^3 were observed in the control groups, including mice treated with AuVNRs, Lipo, AuNRs-Lipo, PBS only, and pre-injection mice, highlighting the superiority of the targeted synergistic therapeutics in reducing tumor size (Figure 5C). Importantly, the successive targeted synergistic therapeutics not only reduced tumor size but also improved the survival time of the treated animals for an extended period, as demonstrated by the 2-month survival rate (Figure 5D). This long-term survival outcome further confirms the good biocompatibility of the administered AuVNR formulations. Besides this, mice underwent tri-weekly assessments for signs of clinical toxicity, morbidity, and mortality. Concerning acute toxicity evaluation, the treated animals did not experience significant changes in body weight, indicating the improved biocompatibility of the nanoparticles (Figure S12). Furthermore, the *in vivo* biosecurity of the injected AuVNRs-DOX was evaluated through histopathological examination by analyzing its effect on major organs such as the heart, lungs, liver, spleen, and kidneys. This analysis was performed by a professional pathologist. After treatment with AuVNRs and AuVNRs-DOX, harvested tissues were fixed in 10% formalin, processed for paraffin sectioning, cut, and stained with hematoxylin and eosin (H&E). These sections showed no tissue damage or abnormality and were comparable with the control group as well as with the AuVNRs alone (Figure S13). Normal macrophages, hepatocytes, portal triads, and central veins were observed in the liver, whereas healthy myofibers and muscle bundles were observed in the heart. Normal glomeruli and tubules of the kidney were also observed. No significant necrosis, pulmonary fibrosis, hydropic degeneration, histological abnormalities, or inflammatory lesions were observed in any of the organ tissues from the mice treated with AuVNRs-DOX, indicating the biocompatibility and safety of the nanotheranostic system.

DISCUSSION

The concept of nanotheranostics has been explored extensively, but the challenge lies in engineering an ideal system that enables site-selective tumor targeting, high accumulation, and localized tumor reduction without harming surrounding healthy tissues.[28,29] For applications in tumor imaging and reduction, numerous metallic and nonmetallic nanotheranostics have been tested thus far.[36] However, they are limited in their precise tumor targeting and accumulation ability.[2,36] Furthermore, these systems tend to accumulate in vital organs for extended periods, potentially leading to harmful side effects. The liver and spleen, in particular, pose significant biological barriers to achieving specific biodistribution of nanoparticles within the body because of factors such as protein corona formation.[37] To overcome these hurdles, the use of cell membrane-coated biomimetic materials has emerged as a promising approach.[18,30] However, challenges such as low reproducibility, scalability, heterogeneous membrane coating, and low stability have limited the application of these formulations.[30] Alternatively, RBC membrane-coated nanoparticles, metallic and nonmetallic, have been proposed as a viable solution because of their ease of preparation and scalability, although they lack specific targeting, biodistribution, and site-selective tumor binding.[17,19]

In this study, we present a unique engineering approach involving bioinspired and biomimetic nanotheranostics composed of CCMVs decorated with AuNRs. This

design offers improved reproducibility and specific biodistribution while avoiding liver accumulation. Additionally, the biomimetic cancer cell nanovesicles coated with nanorods demonstrate site-selective tumor imaging and targeted synergistic therapeutics for solid tumor reduction. Notably, these engineered biomimetic nanotheranostics exhibit superior targeting and penetration abilities in cancer cells and solid tumors, likely because of their inherent surface biomarkers and soft nature. The presence of specific surface markers/proteins on the decorated nanovesicles allows a shorter stay in the liver compared with Lipo-AuNRs. Furthermore, our findings suggest that the enhanced cellular uptake and tumor accumulation under NIR light exposure may be attributed to the photothermal expansion of endothelial cell gaps in leaky blood vessels within solid tumors. However, the precise mechanism behind this phenomenon is not fully understood and extends beyond the scope of this study.

Overall, the designed nanotheranostics demonstrate excellent stability (tested for up to 1 month), dual contrast capabilities for bio-imaging, good biocompatibility with healthy cells and RBCs, and targeted synergistic therapeutic effects for *in vitro* cancer cell death and solid tumor reduction. The controlled body weight and long-term animal survival (lasting months) after therapeutic interventions indicate the potential compatibility and therapeutic safety of synergistic therapy in preclinical models, paving the way for larger animal studies or future clinical trials.

EXPERIMENTAL PROCEDURES

Resource availability

Lead contact

For additional information or resource requests, please get in touch with the lead contact, João Conde, at joao.conde@nms.unl.pt.

Materials availability

No unique reagents were produced during the course of this study.

Data and code availability

All data used and analyzed in this study can be found within the article or its supplemental information. No distinctive codes were created for this research. For further details or data required to re-examine the findings of this article, please contact the lead contact.

Materials

CTAB (99%), gold(III) chloride hydrate ($HAuCl_4$), hydrochloric acid (HCl), ascorbic acid (AA), silver nitrate ($AgNO_3$), hydroquinone, sodium borohydride ($NaBH_4$; 99%), ICG, and MTT were purchased from Sigma-Aldrich. Dulbecco's modified Eagle's medium (DMEM), phosphate-buffered saline (PBS; pH 7.4), dimethyl sulfoxide (DMSO), fetal bovine serum (FBS), 4′,6-diamidino-2-phenylindole (DAPI), and antibiotic-antimycotic solution were obtained from HiMedia. Dipalmitoylphosphatidylcholine (DPPC), 1,2-distearoyl-*sn*-glycero-3-phosphocholine (DSPC) were obtained from Lipoid (Switzerland). Milli-Q (>18.2 MΩ cm) was used for all experiments. Synthesized nanohybrids were characterized through TEM (TEM instrument FEI Tecnai T-20) at low beam voltage (100 kV) exposure. XPS measurements were demonstrated with ULVAC-PHIPHI5000. UV-Vis spectroscopy was performed at a path length of 1 cm using PerkinElmer Lamda-25. Fluorescence spectroscopy was performed using Shimadzu at a slit width of five nm. Dynamic light scattering and zeta potential measurements were recorded by using (DLS)-BI200SM (Brookhaven Instruments, USA). Fluorescence microscopy was carried out by using blue and

red filters from an inverted fluorescence microscope. *In vitro* and *in vivo* fluorescence images were recorded using the *in vivo* imaging system (IVIS) Spectrum (IVIS Spectrum Xenogen), and contrast images were recorded from a clinical CT scanner (100 kVp). An 800-nm NIR laser was used for NIR experiments. Digital pictures were captured with an iPhone12 camera.

Synthesis of plasmonic AuNRs

Small AuNRs were prepared by using the hydroquinone applied seedless growth procedure.[38] Briefly, 1 mL $HAuCl_4$ aqueous solution and 15 mL of CTAB (0.1 M) were mixed with 100 mM aqueous $AgNO_3$ at room temperature (RT) at high speed (900 rpm). Further, 15 μL of HCl was introduced into the above mixture, followed by dropwise addition of 0.1 M hydroquinone under high-speed stirring. After complete mixing (about 30–45 min), freshly prepared ice-cold $NaBH_4$ (0.01 M) solution was injected into the above mixture and stirred for 30 min at high speed (900 rpm). The final mixture was kept overnight in the dark without any disturbance at RT (37°C–39°C). The next day, the prepared AuNRs were washed and collected via multiple centrifugations (5,000 and 10,000 rpm for 20 min) and thoroughly washed with water to remove loosely bound CTAB. On the other hand, large nanorods were prepared by using the seed growth protocol,[9] where 300 μL of $AgNO_3$, 0.5 mM $HauCl_4$, and 100 mM CTAB were mixed in a total of 25 mL of aqueous solution. Further, to prepare the growth solution, 125 μL AA as a reducing agent was introduced into the above mixture. Side by side, 10 mM ice-cold $NaBH_4$, 0.4 mM $HAuCl_4$, and 100 mM CTAB were mixed in a total of 25 mL of an aqueous solution. Further, to prepare the growth solution, 125 μL AA as a reducing agent was introduced into the above mixture. Side by side, 10 mM ice-cold $NaBH_4$, 0.4 mM $HAuCl_4$, and 100 mM CTAB were mixed in a total of 10 mL of the aqueous solution to obtain the seed solution. In the third step, 125 μL of freshly prepared seed solution was introduced into the prepared growth solution under high-speed stirring in the dark. The whole reaction was allowed for 4 h, stirring to initiate the formation of the nanorods at 37°C–39°C, and then kept for a further 24 h without any disturbance. The prepared nanorods were collected via centrifugation and washed 4–5 times (10 min for each time) with Milli-Q water.

Preparation of CCMVs

Nanosized cell membrane vesicles were prepared from 4T1 breast cancer cells. In brief, 4T1 cells (5×10^7 density of cancer cells) were collected via centrifugation (5,000 rpm for 5 min) and washed with PBS (pH 7.4), followed by ice-cold Tris-magnesium buffer washing using the centrifugation method (5,000 rpm for 5 min). The obtained pellet was treated for 2 h via a freeze-thaw process and then diluted with 5 mL of PBS and 2 mL of Tris-magnesium buffer. The prepared suspension was centrifuged at 4°C multiple times (5–6 times) to collect the supernatant and pelleted carefully. Further, the obtained colorless pellet was treated with 1× PBS and 20 mM Tris-magnesium buffer for 1 h and then 0.1× PBS under slow stirring for 12 h. After complete stirring, the mixture was centrifuged. and the pellet was further treated with a hypotonic suspension (a mixture of 20 mM Tris-magnesium buffer, 0.2% HCl, and 0.1× PBS) suspension for 4 h. Now the treated suspension was centrifuged at 5,000 rpm for 5 min, and then we collected supernatant and pellet separately, and the supernatant, which contained small ghost cells, was diluted with 4 mL PBS (pH 7.4). The diluted mixture was further treated with sonication (10 cycles) with 30% intensity and 5 s on/off the pulse and filtered under high pressure to obtain nanosized cell vesicles. NIR-emissive ICG dye (200 μL in the aqueous medium) was loaded during the sonication process.

AuVNRs

The excess CTAB was removed from the prepared AuNR surface (1 mL of CTAB surfactant attached AuNRs) using Milli-Q water washing (15 mL), followed by centrifugation (10,000 rpm for 20 min at 20°C). Collected AuNRs (0.5 mL) were incubated with cell-derived membrane nanovesicles (0.2 mL) at 20°C and 300 rpm for 24 h. Further, nanovesicle-engineered nanorods were collected via centrifugation (10,000 rpm for 20 min at 20°C). To remove unreacted nanovesicles and CTAB surfactant, these nanorods were washed 4 times with Milli-Q water and PBS (pH 7.4) and stored in PBS for further use. To prepare AuVNRs, a mixture of surface-modified AuNRs and CCMVs (1:2 [v/v] in PBS [7.4 pH]) was treated with mild sonication (5 cycles) with 20% intensity and 5-s on/off pulse. The obtained suspension was diluted (10 times) with PBS (pH 7.4) and filtered under high pressure. The engineered nanoparticles were dialyzed (12 kD mw [molecular weight] cutoff) against 2,000 mL DI (deionized) water for 24 h at RT. Dialysate was changed each 6 h. NIR-emissive ICG dye and DOX drug (200 μL in aqueous medium) were loaded into AuVNRs, followed by a sonication process.

ICG dye and DOX drug loading into AuVNRs

For ICG and DOX loading into the AuVNRs, the collected surface-modified AuNRs (0.5 mL) were incubated with (1) ICG dye-loaded cell-derived nanovesicles (0.2 mL) and (2) DOX drug-loaded cell-derived nanovesicles (0.2 mL) at 20°C and 300 rpm for 24 h. The prepared mixtures were sonicated (5 cycles) with 20% intensity and 5 s on/off pulse. Further, emissive nanovesicle-engineered nanorods were collected via centrifugation (10,000 rpm for 20 min at 20°C). To remove unreacted nanovesicles, free dye, and drug, the engineered nanorods were washed 4 times with Milli-Q water and PBS (pH 7.4). The obtained nanoparticles were diluted (10 times) with PBS (pH 7.4) and filtered under high pressure and then were further dialyzed (12 kD mw cutoff) against 2,000 mL DI water for 24 h at RT. During the dialysis process, the dialysate was changed every 6 h and stored in PBS for further use.

Lipo preparation and engineering with AuNRs, ICG, and DOX

Lipos were prepared via the thin film hydration method.[39] The preparation protocol was taken from a procedure reported earlier with some modifications.[28,29] A 5:4:1 ratio of DPPC, DSPC, and cholesterol was dissolved in 10 mL of chloroform at RT and exposed to N_2 gas flow for 2 min. The prepared mixture was carried to solvent evaporation under a rotary evaporator at 100 rpm and 43°C for 1.5 h to obtain a lipid thin film. After complete solvent removal, 10 mL of PBS was added to the obtained lipid film and mixed gently. Now, the prepared aqueous mixture was taken for further film hydration at 45°C for another 2 h and then stored at 4°C overnight. Further, the hydrated lipid films were sonicated (10 cycles with 30% intensity with 5-s on/off pulse) for 10 min to obtain small liposomal vesicles. Further, to prepare Lipo-engineered AuNRs, CTAB-stabilized AuNRs (0.5 mL) were incubated with Lipos (0.2 mL) for 24 h at 20°C. The prepared mixtures were sonicated (10 cycles with 30% intensity with 5-s on/off pulse) for 10 min. Lipo-stabilized nanorods were collected via centrifugation (10,000 rpm for 20 min at 20°C), washed thoroughly with Milli-Q water and PBS (pH 7.4), and then stored in PBS for further use. NIR-emissive ICG dye and DOX (200 μL in aqueous medium) were loaded during the thin film hydration process of Lipos. In brief, ICG dye (0.1 mM) and DOX drug (0.1 mM) were introduced during the film hydration process of the Lipo-stabilized nanorods (10 mL) at 45°C for 2 h. The obtained suspension was sonicated (10 cycles with 30% intensity with 5-s on/off pulse) for 10 min. Further, final nanoparticles were collected via centrifugation (10,000 rpm

for 20 min at 20°C) and washed 4 times with Milli-Q water and PBS (pH 7.4). Unencapsulated nanorods, dye, and drug were removed by washing with PBS, followed by centrifugation and 1-day dialysis (12 kD mw cutoff) at RT.

Aqueous dispersibility, photostability, and phototransduction performance of engineered nanorods

Prepared surface engineered nanorods (1 mg/mL) were mixed in aqueous suspension (aqueous solutions of nanorods were prepared in glass bottles) that was examined for dispersibility at different time points (first day to 30th day), followed by spectroscopic and digital photography measurements at RT. The time-dependent photostability of these nanorods was checked through spectroscopic measurements. Next, an 800-nm NIR laser (1 W power) was applied to evaluate the photothermal response of surface-engineered AuNRs (50 μL volume) for 10 min of NIR light exposure. AuVNRs and AuNRs-Lipo were prepared in aqueous medium at 100 μg/mL concentration, and then temperature response was recorded for 0–10 min upon NIR light exposure.

AuVNRs as a dual nanocontrast agent

The dual contrast ability (X-ray radiocontrast and NIR fluorescence imaging) of AuVNRs-Dye was measured in an aqueous medium at the 2.5–20 μg/mL concentration range. For NIR fluorescence imaging, an IVIS was used at 750 nm of excitation wavelength with 830 nm of emission. In the case of X-ray CT imaging, all X-ray scans were recorded at 100 kVp. Radio contrast values (HU) were measured using RadiAnt DICOM Viewer software. PBS was used as a control contrast for all imaging experiments.

Western blot

4T1 cells were treated with a concentration of desired nanoparticles (150 μM) for 24 h and lysed in lysis buffer, and lysates containing equal amounts of total proteins (40 μg) were resolved by SDS-PAGE and blotted onto nitrocellulose membranes as described by Kumar et al.[40] The levels of apoptosis-specific molecules, such as PARP and Cyclin D1 (Santa Cruz Biotechnology), were analyzed using their specific antibodies. β-Actin was used as a loading control.

In vitro biocompatibility and hemolysis

NIH3T3 healthy cells and RBCs were used for *in vitro* biocompatibility testing. The NIH3T3cell viability test was performed at various concentrations (5–500 μg/mL) using CTAB-attached AuNRs, nanovesicles, Lipos, AuVNRs, AuVNRs-Dye, and AuNRs-Lipo. In brief, a 5×10^4 density of normal NIH3T3 cells was seeded and incubated for 24 h with 5% CO_2 in DMEM (Gibco, Carlsbad, CA, USA) supplemented with 10% FBS and penicillin/streptomycin at 37.0°C. After 24-h incubation, these cultured cells were treated for a further 24 h with 100 μL of each engineered nanohybrid (5–500 μg/mL) mentioned above. After complete incubation treatment, this cell cultured 96 wells were washed off with PBS, and then 20 μL of MTT dye was added for % cell viability measurement. Formed formazan crystals were dissolved using 200 μL of DMSO, and optical absorbance was recorded using a microplate reader (Tecan Infinite 200 PRO). Percent cell viability using an MTT assay was calculated with reference to untreated cells. Next, healthy RBCs were used for hemolysis study.[39] In brief, collected healthy blood (2 mL) was diluted five times with PBS. Diluted blood was centrifuged (1,000 × *g* for 10 min) and washed at least four times with PBS (pH 7.4). Further, collected RBCs were diluted with 20 mL PBS (7.4 pH) and treated with CTAB-attached AuNRs, nanovesicles, Lipos, AuVNRs, AuVNRs-Dye, AuNRs-Lipos, free DOX, AuVNRs-DOX, and AuNRs-Lipo-DOX at various

concentrations (50–500 μg/mL) for 12 h (200 μL of RBCs and 800 μL of nanohybrids from each concentration). After complete treatment, the treated mixture was centrifuged at 1,000 × *g* for 10 min and absorption spectroscopic analysis was done for collected supernatant to measure the absorption of released hemoglobin at 540 nm. The percentage of hemolysis was calculated using the following equation:

$$\text{Hemolysis (\%)} = \frac{(\text{Absorbance of sample} - \text{Absorbance of negative control})}{(\text{Absorbance of positive control} - \text{Absorbance of negative control})} \times 100$$

In vitro cell targeting and targeted synergistic therapeutic

Cancer cell targeting and cellular uptake studies were performed on 4T1 breast cancer cells. In brief, 4T1 breast cancer cells (5×10^4 cells/well) were cultured in DMEM supplemented with 10% FBS and penicillin/streptomycin, followed by 24 h incubation in 5% CO_2 at 37.0°C. When cells were about 80% confluent, 100 μL of AuVNRs-Dye and AuNRs-Lipo-Dye (4.9×10^{12} nanovesicles) were used to treat 4T1 cancer cells. After 6-h incubation, these treated cancer cells were washed with PBS four times to get rid of nanohybrids that were not taken up or untargeted nanohybrids. These cells were fixed with 4% paraformaldehyde, and DAPI was applied to stain cell nuclei. Further, these stained cells were washed with PBS to remove the excess staining, and then cells were mounted with a coverslip using a drop of 70% glycerol on a glass slide. Prepared slides were examined under a fluorescence microscope to check the cell uptake of emissive nanorods. Further, flow cytometry and transmission microscopy measurements were done for cellular uptake studies. Untreated cells were considered control groups for all *in vitro* cell targeting and therapy studies. Next, *in vitro* targeted synergistic therapeutic efficacy was tested on 4T1 cancer cells. For anticancer activity, 4T1 breast cancer cells were seeded at a density of 5×10^4 cells/well in DMEM and cultured, followed by the abovementioned procedure. After 24-h incubation, these cells were treated with 100 μg/mL of CTAB-attached AuNRs, empty nanovesicles, CCMVs-Dye, AuVNRs, AuVNRs-Dye, AuNRs-Lipo, AuNRs-Lipo-DOX, AuVNRs-DOX, and AuVNRs-DOX under NIR light irradiation (800 nm, 10 min for light exposure). Further, these treated cells were left for 24-h incubation. After complete incubation, these treated cells were washed with PBS, and then 20 μL of MTT dye was added, where formazan crystals were dissolved using DMSO, and percent cell viability was calculated with reference to untreated cells (control).

In vivo tumor imaging and bio-distribution studies

Female BALB/c mice were used in all *in vivo* studies with institutional animal ethics committee (IAEC) approval. Breast tumors developed in female BALB/c mice by subcutaneously implanting 5×10^4 4T1 breast cancer cells in the right flank. When tumor growth was significant, 150 μL of AuVNRs-Dye and AuNRs-Lipo-Dye (73.5×10^{11} nanovesicles) were intravenously injected into 4T1 tumor-bearing female BALB/c mice. After injection, tumor imaging was conducted by measuring fluorescence signals from the tumor and whole body using an IVIS Spectrum imaging system at different time points post injection (1 h, 24 h, and 48 h). 750 nm of excitation wavelength with 830 nm of emission was applied during IVIS imaging. Next, X-ray CT scans at 100 kVp were conducted for post-injection tumor-bearing mice at various time points (1 h, 24 h, and 48 h). During imaging, all mice were anesthetized. For bio-distribution measurements, fluorescence signal intensity and radiocontrast values were recorded from major organs (heart, lungs, liver, spleen, intestine, kidneys) and tumors at various time points post injection (1 h, 24 h, and 48 h). At the 48-h time point, treated mice were sacrificed, and tumors along with major organs were harvest for *ex vivo*

imaging using X-ray CT. Several analyses were made for bio-distribution and tumor imaging.

Targeted synergistic therapeutic efficacy for solid tumor reduction

For targeted solid tumor therapeutic efficacy, various theranostic nanoparticles, such as AuVNRs, Lipos, AuVNRs-DOX, AuVNRs-DOX under NIR, AuNRs-Lipo, and AuNRs-Lipo-DOX, were intravenously injected into 4T1 tumor-bearing female mice (4 mice per group) and compared with control (pre-injected, as no injection and PBS-treated animals). 1 h post-injection, these animals were exposed to NIR light (800 nm for 10 min), which was repeated for five therapeutic courses with 3-day time intervals (a 150-μL dose was administered for each therapeutic course). Various qualitative and quantitative analyses of tumor size, volume, weight, and animal survival were performed during *in vivo* cancer therapy studies.

Statistics

For statistical analysis, all experiments were performed in triplicate. All data were analyzed and plotted using OriginPro 8 and Sigma Plot 10.0 software. Significant observations between different groups were calculated by t test.

Additional experimental information

Different data of designed nanotheranostics are included in the Supplemental experimental procedures. Supporting data, such as surface charge zeta potential, dispersion, XPS, absorption spectra, simulation information and data, photothermal experiment details, drug release kinetics patterns, IVIS, cell imaging, hemolysis, X-ray CT tumor imaging, blood circulation lifetime, *in vivo* tumor therapeutics, body weight measurements, fluorescence-activated cell sorting (FACS), and calculated pixel intensity are included.

SUPPLEMENTAL INFORMATION

Supplemental information can be found online at https://doi.org/10.1016/j.xcrp.2023.101648.

ACKNOWLEDGMENTS

J.C. and B.M. acknowledge European Research Council grant agreement 848325. R.P. would like to thank the Director, Indian Institute of Technology (BHU), Varanasi and the School of Biochemical Engineering, IIT (BHU) for support during preparation of this manuscript. We thank the Trident Diagnostics Center and staff for imaging and laser studies and NCCS, Pune for *in vivo* facilities. We would like to thank Prof. Rohit Srivastava and Dr. Sumit for their kind support. We extend our thanks to the School of Biotechnology and Kalinga Institute of Medical Sciences, KIIT, Institute of Eminence, Bhubaneswar. We dedicate this article to the memory of the late Prof. Sanjiv Sam Gambhir, a molecular imaging scientist. Figures/schemes were created with BioRender.

AUTHOR CONTRIBUTIONS

J.C. and R.P. conceived the idea. M.G., G.C.K., R.P., and J.C. designed the experiments. M.G., G.C.K., R.P., and N.G. performed *in vivo* imaging and therapeutics studies. B.P. and E.H.A.W. conducted the western blots. B.P. and H.Q. performed the simulation studies. R.P., B.M., and J.C. wrote the paper. All authors contributed to final editing and multiple revisions of the present manuscript.

DECLARATION OF INTERESTS

J.C. is a co-founder and shareholder of TargTex S.A. R.P. is part of national and international patents related to lipid, gold, silica, and erythrocyte-based nanoparticles.

Received: April 17, 2023
Revised: September 7, 2023
Accepted: September 28, 2023
Published: October 18, 2023

REFERENCES

1. Zhou, J., Rao, L., Yu, G., Cook, T.R., Chen, X., and Huang, F. (2021). Supramolecular cancer nanotheranostics. Chem. Soc. Rev. *50*, 2839–2891. https://doi.org/10.1039/D0CS00011F.

2. Wong, X.Y., Sena-Torralba, A., Álvarez-Diduk, R., Muthoosamy, K., and Merkoçi, A. (2020). Nanomaterials for Nanotheranostics: Tuning Their Properties According to Disease Needs. ACS Nano *14*, 2585–2627. https://doi.org/10.1021/acsnano.9b08133.

3. Mendes, B.B., Sousa, D.P., Conniot, J., and Conde, J. (2021). Nanomedicine-based strategies to target and modulate the tumor microenvironment. Trends Cancer *7*, 847–862. https://doi.org/10.1016/j.trecan.2021.05.001.

4. Bort, G., Lux, F., Dufort, S., Crémillieux, Y., Verry, C., and Tillement, O. (2020). EPR-mediated tumor targeting using ultrasmall-hybrid nanoparticles: From animal to human with theranostic AGuIX nanoparticles. Theranostics *10*, 1319–1331.

5. Prasad, R., Jain, N.K., Conde, J., and Srivastava, R. (2020). Localized nanotheranostics: recent developments in cancer nanomedicine. Mater. Today Adv. *8*, 100087. https://doi.org/10.1016/j.mtadv.2020.100087.

6. Chen, H., Zhang, W., Zhu, G., Xie, J., and Chen, X. (2017). Rethinking cancer nanotheranostics. Nat. Rev. Mater. *2*, 17024. https://doi.org/10.1038/natrevmats.2017.24.

7. Liu, X., Yang, Y., Wang, X., Liu, X., Cheng, H., Wang, P., Shen, Y., Xie, A., and Zhu, M. (2021). Self-assembled Au4Cu4/Au25 NCs@liposome tumor nanotheranostics with PT/fluorescence imaging-guided synergetic PTT/PDT. J. Mater. Chem. B *9*, 6396–6405. https://doi.org/10.1039/D1TB01092A.

8. Akakuru, O.U., Liu, C., Iqbal, M.Z., Dar, G.I., Yang, G., Qian, K., Nosike, E.I., Xing, J., Zhang, Z., Li, Y., et al. (2020). A Hybrid Organo-Nanotheranostic Platform of Superlative Biocompatibility for Near-Infrared-Triggered Fluorescence Imaging and Synergistically Enhanced Ablation of Tumors. Small *16*, 2002445. https://doi.org/10.1002/smll.202002445.

9. Zhao, X., Yang, C.-X., Chen, L.-G., and Yan, X.-P. (2017). Dual-stimuli responsive and reversibly activatable theranostic nanoprobe for precision tumor-targeting and fluorescence-guided photothermal therapy. Nat. Commun. *8*, 14998. https://doi.org/10.1038/ncomms14998.

10. Steichen, S.D., Caldorera-Moore, M., and Peppas, N.A. (2013). A review of current nanoparticle and targeting moieties for the delivery of cancer therapeutics. Eur. J. Pharm. Sci. *48*, 416–427. https://doi.org/10.1016/j.ejps.2012.12.006.

11. van der Meel, R., Sulheim, E., Shi, Y., Kiessling, F., Mulder, W.J.M., and Lammers, T. (2019). Smart cancer nanomedicine. Nat. Nanotechnol. *14*, 1007–1017. https://doi.org/10.1038/s41565-019-0567-y.

12. Prasad, R., and Conde, J. (2022). Bioinspired soft nanovesicles for site-selective cancer imaging and targeted therapies. WIREs Nanomed. Nanobiotechnol. *14*, e1792. https://doi.org/10.1002/wnan.1792.

13. Fang, R.H., Kroll, A.V., Gao, W., and Zhang, L. (2018). Cell Membrane Coating Nanotechnology. Adv. Mater. *30*, 1706759. https://doi.org/10.1002/adma.201706759.

14. Liu, L., Bai, X., Martikainen, M.-V., Kårlund, A., Roponen, M., Xu, W., Hu, G., Tasciotti, E., and Lehto, V.-P. (2021). Cell membrane coating integrity affects the internalization mechanism of biomimetic nanoparticles. Nat. Commun. *12*, 5726. https://doi.org/10.1038/s41467-021-26052-x.

15. Wan, X., Zhang, S., Wang, F., Fan, W., Wu, C., Mao, K., Wang, H., Hu, Z., Yang, Y.-G., and Sun, T. (2018). Red blood cell-derived nanovesicles for safe and efficient macrophage-targeted drug delivery in vivo. Biomater. Sci. *7*, 187–195. https://doi.org/10.1039/C8BM01258J.

16. Ferrel, C., Rayamajhi, S., Nguyen, T., Marasini, R., Saravanan, T., Deba, F., and Aryal, S. (2021). Re-engineering a Liposome with Membranes of Red Blood Cells for Drug Delivery and Diagnostic Applications. ACS Appl. Bio Mater. *4*, 6974–6981. https://doi.org/10.1021/acsabm.1c00643.

17. Xiong, J., Wu, M., Chen, J., Liu, Y., Chen, Y., Fan, G., Liu, Y., Cheng, J., Wang, Z., Wang, S., et al. (2021). Cancer-Erythrocyte Hybrid Membrane-Camouflaged Magnetic Nanoparticles with Enhanced Photothermal-Immunotherapy for Ovarian Cancer. ACS Nano *15*, 19756–19770. https://doi.org/10.1021/acsnano.1c07180.

18. Ren, X., Zheng, R., Fang, X., Wang, X., Zhang, X., Yang, W., and Sha, X. (2016). Red blood cell membrane camouflaged magnetic nanoclusters for imaging-guided photothermal therapy. Biomaterials *92*, 13–24. https://doi.org/10.1016/j.biomaterials.2016.03.026.

19. Ben-Akiva, E., Meyer, R.A., Yu, H., Smith, J.T., Pardoll, D.M., and Green, J.J. (2020). Biomimetic anisotropic polymeric nanoparticles coated with red blood cell membranes for enhanced circulation and toxin removal. Sci. Adv. *6*, eaay9035. https://doi.org/10.1126/sciadv.aay9035.

20. Sindhwani, S., Syed, A.M., Ngai, J., Kingston, B.R., Maiorino, L., Rothschild, J., MacMillan, P., Zhang, Y., Rajesh, N.U., Hoang, T., et al. (2020). The entry of nanoparticles into solid tumours. Nat. Mater. *19*, 566–575. https://doi.org/10.1038/s41563-019-0566-2.

21. Izci, M., Maksoudian, C., Manshian, B.B., and Soenen, S.J. (2021). The Use of Alternative Strategies for Enhanced Nanoparticle Delivery to Solid Tumors. Chem. Rev. *121*, 1746–1803. https://doi.org/10.1021/acs.chemrev.0c00779.

22. Lin, Z.P., Nguyen, L.N.M., Ouyang, B., MacMillan, P., Ngai, J., Kingston, B.R., Mladjenovic, S.M., and Chan, W.C.W. (2022). Macrophages Actively Transport Nanoparticles in Tumors After Extravasation. ACS Nano *16*, 6080–6092. https://doi.org/10.1021/acsnano.1c11578.

23. Kingston, B.R., Lin, Z.P., Ouyang, B., MacMillan, P., Ngai, J., Syed, A.M., Sindhwani, S., and Chan, W.C.W. (2021). Specific Endothelial Cells Govern Nanoparticle Entry into Solid Tumors. ACS Nano *15*, 14080–14094. https://doi.org/10.1021/acsnano.1c04510.

24. Rastinehad, A.R., Anastos, H., Wajswol, E., Winoker, J.S., Sfakianos, J.P., Doppalapudi, S.K., Carrick, M.R., Knauer, C.J., Taouli, B., Lewis, S.C., et al. (2019). Gold nanoshell-localized photothermal ablation of prostate tumors in a clinical pilot device study. Proc. Natl. Acad. Sci. USA *116*, 18590–18596. https://doi.org/10.1073/pnas.1906929116.

25. Min, Y., Caster, J.M., Eblan, M.J., and Wang, A.Z. (2015). Clinical Translation of Nanomedicine. Chem. Rev. *115*, 11147–11190. https://doi.org/10.1021/acs.chemrev.5b00116.

26. Gilam, A., Conde, J., Weissglas-Volkov, D., Oliva, N., Friedman, E., Artzi, N., and Shomron, N. (2016). Local microRNA delivery targets Palladin and prevents metastatic breast cancer. Nat. Commun. *7*, 12868. https://doi.org/10.1038/ncomms12868.

27. Zhan, M., Yu, X., Zhao, W., Peng, Y., Peng, S., Li, J., and Lu, L. (2022). Extracellular matrix-degrading STING nanoagonists for mild NIR-II photothermal-augmented chemodynamic-immunotherapy. J. Nanobiotechnology *20*, 23. https://doi.org/10.1186/s12951-021-01226-3.

28. Prasad, R., Chauhan, D.S., Yadav, A.S., Devrukhkar, J., Singh, B., Gorain, M., Temgire, M., Bellare, J., Kundu, G.C., and Srivastava, R. (2018). A biodegradable fluorescent nanohybrid for photo-driven tumor diagnosis and tumor growth inhibition. Nanoscale *10*, 19082–19091. https://doi.org/10.1039/C8NR05164J.

29. Prasad, R., Jain, N.K., Yadav, A.S., Chauhan, D.S., Devrukhkar, J., Kumawat, M.K., Shinde, S., Gorain, M., Thakor, A.S., Kundu, G.C., et al. (2020). Liposomal nanotheranostics for multimode targeted in vivo bioimaging and near-infrared light mediated cancer therapy. Commun. Biol. *3*, 284. https://doi.org/10.1038/s42003-020-1016-z.

30. Bose, R.J.C., Uday Kumar, S., Zeng, Y., Afjei, R., Robinson, E., Lau, K., Bermudez, A., Habte, F., Pitteri, S.J., Sinclair, R., et al. (2018). Tumor Cell-Derived Extracellular Vesicle-Coated Nanocarriers: An Efficient Theranostic Platform for the Cancer-Specific Delivery of Anti-miR-21 and Imaging Agents. ACS Nano *12*, 10817–10832. https://doi.org/10.1021/acsnano.8b02587.

31. Wang, Y., Black, K.C.L., Luehmann, H., Li, W., Zhang, Y., Cai, X., Wan, D., Liu, S.-Y., Li, M., Kim, P., et al. (2013). Comparison Study of Gold Nanohexapods, Nanorods, and Nanocages for Photothermal Cancer Treatment. ACS Nano *7*, 2068–2077. https://doi.org/10.1021/nn304332s.

32. Conde, J., Oliva, N., Zhang, Y., and Artzi, N. (2016). Local triple-combination therapy results in tumour regression and prevents recurrence in a colon cancer model. Nat. Mater. *15*, 1128–1138. https://doi.org/10.1038/nmat4707.

33. Mendes, B.B., Conniot, J., Avital, A., Yao, D., Jiang, X., Zhou, X., Sharf-Pauker, N., Xiao, Y., Adir, O., Liang, H., et al. (2022). Nanodelivery of nucleic acids. Nat. Rev. Methods Primers *2*, 24. https://doi.org/10.1038/s43586-022-00104-y.

34. Dong, H., Gao, Y., Huang, X., and Wu, X. (2022). Synthesis of sialic acid conjugates of the clinical near-infrared dye as next-generation theranostics for cancer phototherapy. J. Mater. Chem. B *10*, 927–934. https://doi.org/10.1039/D1TB02693C.

35. Bindra, A.K., Sreejith, S., Prasad, R., Gorain, M., Thomas, R., Jana, D., Nai, M.H., Wang, D., Tharayil, A., Kundu, G.C., et al. (2022). A Plasmonic Supramolecular Nanohybrid as a Contrast Agent for Site-Selective Computed Tomography Imaging of Tumor. Adv. Funct. Mater. *32*, 2110575. https://doi.org/10.1002/adfm.202110575.

36. Kunjachan, S., Ehling, J., Storm, G., Kiessling, F., and Lammers, T. (2015). Noninvasive Imaging of Nanomedicines and Nanotheranostics: Principles, Progress, and Prospects. Chem. Rev. *115*, 10907–10937. https://doi.org/10.1021/cr500314d.

37. Poon, W., Zhang, Y.-N., Ouyang, B., Kingston, B.R., Wu, J.L.Y., Wilhelm, S., and Chan, W.C.W. (2019). Elimination Pathways of Nanoparticles. ACS Nano *13*, 5785–5798. https://doi.org/10.1021/acsnano.9b01383.

38. Chen, Y.-S., Zhao, Y., Yoon, S.J., Gambhir, S.S., and Emelianov, S. (2019). Miniature gold nanorods for photoacoustic molecular imaging in the second near-infrared optical window. Nat. Nanotechnol. *14*, 465–472. https://doi.org/10.1038/s41565-019-0392-3.

39. Prasad, R., Yadav, A.S., Gorain, M., Chauhan, D.S., Kundu, G.C., Srivastava, R., and Selvaraj, K. (2019). Graphene Oxide Supported Liposomes as Red Emissive Theranostics for Phototriggered Tissue Visualization and Tumor Regression. ACS Appl. Bio Mater. *2*, 3312–3320. https://doi.org/10.1021/acsabm.9b00335.

40. Kumar, D., Haldar, S., Gorain, M., Kumar, S., Mulani, F.A., Yadav, A.S., Miele, L., Thulasiram, H.V., and Kundu, G.C. (2018). Epoxyazadiradione suppresses breast tumor growth through mitochondrial depolarization and caspase-dependent apoptosis by targeting PI3K/Akt pathway. BMC Cancer *18*, 52.